

On the High Energy Emission of the Short GRB 090510

Hao-Ning He^{1,2,4,5}, Xue-Feng Wu^{2,3,4}, Kenji Toma^{2,4}, Xiang-Yu Wang^{1,5} and Peter Mészáros^{2,4}

ABSTRACT

Long-lived high-energy ($> 100\text{MeV}$) emission, a common feature of most Fermi-LAT detected gamma-ray burst, is detected up to $\sim 10^2$ s in the short GRB 090510. We study the origin of this long-lived high-energy emission, using broad-band observations including X-ray and optical data. We confirm that the late > 100 MeV, X-ray and optical emission can be naturally explained via synchrotron emission from an adiabatic forward shock propagating into a homogeneous ambient medium with low number density. The Klein-Nishina effects are found to be significant, and effects due to jet spreading and magnetic field amplification in the shock appear to be required. Under the constraints from the low-energy observations, the adiabatic forward shock synchrotron emission is consistent with the later-time ($t \gtrsim 2\text{s}$) high-energy emission, but falls below the early-time ($t < 2\text{s}$) high energy emission. Thus we argue that an extra high energy component is needed at early times. A standard reverse shock origin is found to be inconsistent with this extra component. Therefore, we attribute the early part of the high-energy emission ($t \lesssim 2\text{s}$) to the prompt component, and the long-lived high energy emission ($t \gtrsim 2\text{s}$) to the adiabatic forward shock synchrotron afterglow radiation. This avoids the requirement for an extremely high initial Lorentz factor.

Subject headings: gamma-ray burst: general, gamma-ray burst: individual: 090510, radiation mechanism: non-thermal

¹Department of Astronomy, Nanjing University, Nanjing 210093, China

²Department of Astronomy & Astrophysics, Department of Physics, Pennsylvania State University, 525 Davey Lab, University Park, PA 16802

³Purple Mountain Observatory, Chinese Academy of Sciences, Nanjing 210008, China

⁴Center for Particle Astrophysics, Pennsylvania State University, 104 Davey Lab, University Park, PA 16802

⁵Key Laboratory of Modern Astronomy and Astrophysics (Nanjing University), Ministry of Education, Nanjing 210093, China

1. INTRODUCTION

Gamma-ray bursts (GRBs) are the most luminous explosions in the universe. Their basic scenario based on the emission from extremely relativistic outflows with bulk Lorentz factors $10^2 - 10^3$ and isotropic energies of $10^{48} - 10^{55}$ erg has been tested, although many questions remain open. The Fermi satellite has advanced our knowledge of GRBs significantly, while raising some new puzzles. During its first ~ 2 yr of operation as of July 27th, 2010, Fermi has observed 19 GRBs with photons detected in the LAT (Large Area Telescope) instrument. These observations reveal three new properties (Granot et al. 2010; Abdo et al. 2009d,c, 2010, 2009b,a; Ackermann et al. 2010a,b; Fermi-LAT & Fermi-GBM collaborations 2011): i) A delayed high energy emission, e.g., in GRB 080916C, GRB 081024B, GRB 090510, GRB 090902B and GRB 090926A¹. ii) A temporally extended high energy emission: at least 10 of the first 19 Fermi LAT GRBs have long-lived high energy emission, lasting much longer than the burst duration in the sub-MeV band (which declines very rapidly); in 4 out of 10 GRBs, the long-lived LAT light curves have a relatively steeper slope, for example, -1.33 ± 0.08 for GRB 080916C, -1.70 ± 0.08 for GRB 090510, -1.40 ± 0.06 for GRB 090902B, -2.05 ± 0.14 for GRB 090926A according to Zhang et al. (2010). iii) A deviation from a pure Band spectral function, showing an extra component in GRB 090510, GRB 090902B, GRB 090926A. These are among the brightest bursts, but the observations are compatible with the hypothesis of having such a component also in the other, less bright bursts, where it is harder to detect (Granot et al. 2010).

Among these 19 Fermi LAT GRBs, GRB 090510 is a short, hard burst, with a duration $T_{90} = 0.30 \pm 0.07$ s (De Pasquale et al. 2010; Ukwatta et al. 2009), located at a redshift $z = 0.903 \pm 0.003$ (McBreen et al. 2010; Rau et al. 2009). It has been detected by Fermi (Guiriec et al. 2009; Ackermann et al. 2010b), AGILE (Longo et al. 2009), Swift (Hoversten et al. 2009), Konus-Wind (Golenetskii et al. 2009) and Suzaku (Ohmori et al. 2009). Thus, a large amount of high-quality broadband information is available on this burst, including optical, X-ray, MeV and GeV emission. The Swift BAT instrument triggered on GRB 090510 at $T_0^{\text{BAT}} = 00 : 23 : 00.4$ UT, May 10th, 2009 (Hoversten et al. 2009), while the GBM instrument onboard Fermi triggered on at $T_0^{\text{F}} = 00 : 22 : 59.97$ UT, May 10th, 2009 (Abdo et al. 2009b). Thus, there is a deviation between the two trigger times, which is $\Delta T_0 = T_0^{\text{BAT}} - T_0^{\text{F}} = 0.43$ s. Hereafter we adopt the BAT trigger time T_0^{BAT} as a natural start time T_0 for computing the afterglow evolution, this being the onset of the main burst.

The high energy emission of GRB 090510 has all three of the new features we summarized

¹The first > 100 MeV photons arrive later than the first lower energy photons detected by GBM (Gamma-ray Burst Monitor).

above: i) the bulk of the photons above 30 MeV arrive 253 ± 34 ms later than those below 1MeV (Abdo et al. 2009b); ii) the high energy emission above 100MeV shows a simple power law decay lasting 200s with a temporal decay index $\alpha_{\text{LAT}} = 1.38 \pm 0.07$ (De Pasquale et al. 2010)²; iii) the time-integrated spectrum from $T_0 + 0.07$ s to $T_0 + 0.57$ s is best fit by a Band function and a power-law spectrum (Abdo et al. 2009b); the extra power-law component photon index of -1.62 ± 0.03 can fit the data well up to the highest-energy (31GeV) photon (Abdo et al. 2009b).

The XRT observations alone give a spectral index 0.57 ± 0.08 (Hoversten et al. 2009), while a detailed analysis of the temporal XRT emission combined with the LAT emission indicates a spectral index β_X ranging from 0.51 to 0.81(De Pasquale et al. 2010), and a temporal decay index $\alpha_{X,1} = 0.74 \pm 0.03$ before a break time $t_{X,b} = 1.43$ ks, which subsequently steepens to $\alpha_{X,2} = 2.18 \pm 0.10$. The optical emission initially rises with a temporal index $\alpha_{\text{opt},1} = -0.5^{+0.11}_{-0.13}$, and after a break time $t_{\text{opt},b} = 1.58^{+0.46}_{-0.37}$ ks it decays with a temporal index $\alpha_{\text{opt},2} = 1.13^{+0.11}_{-0.10}$ (De Pasquale et al. 2010).

Most of the models aimed at explaining the long-lived high energy emission of GRB 090510 have favored the view that the high energy photons arise from the afterglow emission, being generated via synchrotron emission in the external forward shock (e.g., Kumar & Barniol Duran 2009, 2010; Corsi et al. 2010; De Pasquale et al. 2010; Gao et al. 2009; Ghirlanda et al. 2010; Ghisellini et al. 2010; Wang et al. 2010; Razzaque 2010) . This explanation is fairly natural, since an external forward shock model can account for, at least in its gross features, not only for the observed delay of the > 100 MeV photons, which corresponds to the deceleration time-scale of the relativistic ejecta, but also for the long lasting > 100 MeV emission, which can be attributed to the power-law decay of the synchrotron external forward shock emission (Kumar & Barniol Duran 2009, 2010). However, various of the above cited authors use somewhat different readings of the publicly available spectral and temporal slope data, which lead them to favor different explanations for the rapid decay of the long-lived high energy emission, falling into five different classes of models as follows.

One set of models interprets the LAT emission as synchrotron emission of electrons accelerated in a standard adiabatic ISM forward shock (Kumar & Barniol Duran 2009, 2010; Corsi et al. 2010; De Pasquale et al. 2010). These authors argue that they can explain the LAT, X-ray, and optical data with plausible parameter values (and we revisit these arguments below). However, these authors did not perform a complete enough study to confirm whether the whole LAT data including the first 1 second can be explained by this type of models. Kumar & Barniol Duran (2009, 2010) fit the late LAT data as $F_\nu \propto t^{-1.2}$, but do not give

²Here we use the convention $F_\nu \propto t^{-\alpha\nu^{-\beta}}$.

much significance to the early-time LAT data. Corsi et al. (2010) fit the whole LAT data as $t^{-1.3}$, which seems to explain the early-time LAT data but exceeds the 2σ upper limits at late times ($\sim 100 - 1000s$). De Pasquale et al. (2010) suggest a steeper decay slope of the high energy emission (evolving as $t^{-1.38}$) for the whole LAT data by taking a larger electron distribution index $p = 2.5$, but they don't take into account in sufficient depth the early-time LAT data ($t < 1s$), which is necessary in order to conclude what is the origin of the entire LAT emission (see more discussion in Section 6).

Other models, e.g., Neamus (2010) attribute the high-energy photons to synchrotron-self-Compton scattering (SSC) from an adiabatic forward shock propagating into a wind-like medium; this, however, requires an extremely small magnetic energy fraction $\epsilon_B = 10^{-10}$. Another, different adiabatic forward shock model analyses in greater detail the Klein-Nishina (KN) effects on the high energy inverse Compton process (Wang et al. 2010). For some reasonable parameters, the KN effect, as it weakens in time, results in the synchrotron high energy emission being increasingly suppressed by the SSC cooling, which steepens the synchrotron high energy emission decay slope by a factor as large as 0.5. A fourth model views the high-energy emission as decaying proportional to $t^{-1.5}$, which is interpreted as being caused by synchrotron emission of electrons accelerated in a forward shock in the radiative, rather than adiabatic, regime. For this, the electron population must be significantly enriched, which is attributed to pair production between back-scattering photons and prompt outward-going photons (Ghisellini et al. 2010). This model explains the high energy emission without considering the constraints from lower energy, e.g., GBM band, XRT band and UVOT band emission, and the pair formation becomes inefficient at shock radii larger than $10^{16}cm$, while $R_{dec} \gg 10^{16}cm$ for this burst (see §4). A fifth type of model for the afterglow of this burst (and others) is a hadronic model (Razzaque 2010), which explains the high energy emission as proton synchrotron emission, while attributing the low energy emission to electron synchrotron emission from a forward external shock. This requires a large total kinetic energy $E_{k,iso} = 2 \times 10^{55}erg^3$, with a low radiation efficiency and an extremely small fraction of electron energy $\epsilon_e = 10^{-4}$.

In this article, we re-examine the first set of models (the standard adiabatic forward shock model) in significantly greater detail than hitherto. We present detailed arguments indicating that it is most likely that the forward shock synchrotron emission can only explain the LAT emission from $\sim 2 - 3$ sec. This conclusion disfavors the external shock origin of the early-time LAT emission (Ghisellini et al. 2010; Kumar & Barniol Duran 2009), but supports the suggestions that it is related to the prompt emission (Corsi et al. 2010; De Pasquale

³Similarly large energies are required for hadronic models of the prompt emission of this burst (Asano et al. 2009).

et al. 2010). In § 2, we examine the XRT and UVOT observations, and set up a model of the long-lived emission based on synchrotron emission from electrons accelerated in a forward shock in a uniform ambient environment, including these X-ray and optical/UV observations. We discuss the impact of the Klein-Nishina effects on the high energy emission, under the constraints imposed by the lower energy observations, which are found to be significant for suppressing the SSC cooling. In §3 we use a semi-analytical model to calculate the development of the dynamical quantities of the forward shock across the deceleration time and into the self-similar phase, and use this to calculate the radiation properties of the long-lived high energy emission produced by synchrotron emission. We find a reasonable set of parameters which can explain most of the late afterglow, except for the six earliest LAT data points in the light curve. In §4 we check several possibilities for the origin of this early high energy emission at times $t < 2 - 3$ s. In §5 we discuss the possibility of the line-of-sight prompt emission as the origin of the early-time high-energy emission. In §6 we discuss our conclusions concerning the most probable origin of the high energy emission from the short GRB 090510.

2. Forward shock model

2.1. Constraints from low energy emission of GRB 090510

The afterglow emission of GRB is generally well explained by synchrotron emission from electrons accelerated by the shock produced during a spherical relativistic shell colliding with an external medium. From the spectral index $\beta_X \sim 0.51 - 0.81$ and the light curve slope $\alpha_{X,1} = 0.74 \pm 0.03$ (De Pasquale et al. 2010), the closure relation for the X-ray afterglow $\alpha_{X,1} - 1.5\beta_X$ ranges from -0.51 to 0.01 , suggesting a slow-cooling ISM external forward shock model with $\nu_m^f < \nu_X < \nu_c^f$ ⁴, which implies that the decay index of the X-ray light curve before the jet break is $\alpha_{X,1} = 3(p - 1)/4$ and the X-ray spectral index is $\beta_X = (p - 1)/2$ (Sari et al. 1998).⁵ From the spectral index we can get a constraint on p which is $p \sim 2.0 - 2.6$. In the external shock model, the break seen in X-ray light curve can be explained as a jet break.

⁴Hereafter we use the subscripts or superscripts ‘f’ and ‘r’ to represent the quantities of the forward-shocked and reverse-shocked regions, respectively, and we use the convention $Q_x = Q/10^x$ in cgs units throughout the paper.

⁵ The closure relation $\alpha_{X,1} - 1.5\beta_X = -0.5$ indicates the slow/fast-cooling ISM/wind external forward shock model with $\nu_X > \nu_c^f$ and the spectral index $\beta_X = p/2$, but this implies $p = 1.6 < 2.0$, which is not favored by numerical simulations of shock acceleration (e.g., Achterberg et al. (2001)) or by observational data of general GRB afterglows (Freedman & Waxman 2001).

We assume that the jet expands sideways (Sari et al. 1999). In this case the X-ray light curve slope steepens gradually from $-3(p-1)/4$ to $-p$, so that we have $3(p-1)/4 < \alpha_{X,2} < p$, which is reduced to $2.2 < p < 3.9$ by taking $\alpha_{X,2} \sim 2.2$. Combining the above two constraints we have $2.2 \lesssim p \lesssim 2.6$. Then the X-ray decay slope before the break should be $0.9 \lesssim \alpha_{X,1} \lesssim 1.2$, which can be acceptable if we take into account the observed fluctuation of the X-ray flux, as the light curves we will show below.

For the rising portion of the optical light curve before the break time, it is natural to assume that the optical band is below ν_m^f , which induces an optical light curve slope of $t^{1/2}$ (Sari et al. 1998; Kumar & Barniol Duran 2010). The predicted spectral slope $\nu^{1/3}$ is consistent with the observations within the large error bars (De Pasquale et al. 2010). Thus, one can try to explain both the X-ray emission and the optical emission before the break time with synchrotron emission of electrons accelerated in an adiabatic external forward shock with the assumptions $\nu_{\text{opt}} < \nu_m^f$ and $\nu_m^f < \nu_X < \nu_c^f$. Then, assuming that the optical band is in the regime of $\nu_m^f < \nu_{\text{opt}} < \nu_c^f$ after the break time, the slope of the optical post-break light curve is the same as that of the X-ray light curve.

In the analytical calculations of this section, we assume that the self-similar phase conditions have been established, and for simplicity we neglect the structure of the shock wave, considering a spherical shock with a total isotropic energy E and a Lorentz factor Γ . At late times, the adiabatic dynamical evolution of the spherical shock is in the Blandford & Mckee self-similar phase, where $E = 16\pi\Gamma^2 R^3 n m_p c^2 / 17$ is constant and the scaling law of the shock wave is $\Gamma \propto R^{-3/2}$ (Blandford & McKee 1976). The shock propagates a distance $\delta R \sim 2\Gamma^2 c \delta t / (1+z)$ during the small observing time δt (Sari 1997), and integrating this and using the scaling law, one obtains $t = (1+z)R/8\Gamma^2 c$.

According to Sari et al. (1998), the cooling and minimum Lorentz factors of the electrons in the forward shock depend on the total isotropic kinetic energy E , the number density of the external environment n , and the fraction of the electron energy and magnetic field energy ϵ_{ef} and ϵ_{Bf} , which can be expressed as

$$\gamma_c^f = \frac{6\pi(1+z)m_e c}{\sigma_T B'^2 \Gamma t} = 2.0 \times 10^8 \epsilon_{Bf,-4}^{-1} E_{53.5}^{-3/8} n_{-4}^{-5/8} t_2^{1/8} [1 + Y(\gamma_c^f)]^{-1} \quad (1)$$

and

$$\gamma_m^f = \epsilon_{ef} \frac{p-2}{p-1} \frac{m_p}{m_e} \Gamma = 9.0 \times 10^4 \epsilon_{ef,-0.4} E_{53.5}^{1/8} n_{-4}^{-1/8} t_2^{-3/8} g_p, \quad (2)$$

respectively, where

$$B' = (32\pi\epsilon_{Bf}\Gamma^2 n m_p c^2)^{1/2} = 1.4 \times 10^{-2} \epsilon_{Bf,-4}^{1/2} E_{53.5}^{1/8} n_{-4}^{3/8} t_2^{-3/8} G \quad (3)$$

and $g_p \equiv 3(p-2)/(p-1)$, p is the power-law index of the electron energy distribution, $Y(\gamma_c^f)$ is the Compton parameter of the electrons with Lorentz factor γ_c^f , and σ_T is Thomson cross

section. The cooling and minimum frequencies of electrons are

$$h\nu_c^f = h \frac{q_e B'}{2\pi m_e c} (\gamma_c^f)^2 \Gamma = 2.3 \times 10^9 [1 + Y(\gamma_c^f)]^{-2} \epsilon_{Bf,-4}^{-3/2} E_{53.5}^{-1/2} n_{-4}^{-1} t_2^{-1/2} \text{eV} \quad (4)$$

and

$$h\nu_m^f = h \frac{q_e B'}{2\pi m_e c} (\gamma_m^f)^2 \Gamma = 5.0 \times 10^2 \epsilon_{ef,-0.4}^2 \epsilon_{Bf,-4}^{1/2} E_{53.5}^{1/2} t_2^{-3/2} g_p^2 \text{eV}, \quad (5)$$

respectively. The peak flux density of the forward shock synchrotron emission is

$$F_{\text{max}}^f = \frac{(1+z) N_e^f m_e c^2 \sigma_T B' \Gamma}{12\pi q_e d_L^2} = 137 \epsilon_{Bf,-4}^{1/2} E_{53.5} n_{-4}^{1/2} \mu\text{Jy}, \quad (6)$$

where the total number of the electrons that the forward shock swept up is $N_e^f = \frac{16}{17} \pi R^3 n = 1.5 \times 10^{51} E_{53.5}^{3/4} n_{-4}^{1/4} t_2^{3/4}$, and d_L is the luminosity distance.

We get two constraints from the UVOT and XRT data as follows:

(i) The optical flux density is about $20 \mu\text{Jy}$ at $t \sim 100\text{s}$ (De Pasquale et al. 2010), which indicates that

$$F_{\text{opt}}(t = 100\text{s}) \simeq F_{\text{max}}^f \left(\frac{4.5\text{eV}}{h\nu_m^f} \right)^{1/3} = 28.5 \epsilon_{ef,-0.4}^{-2/3} \epsilon_{Bf,-4}^{1/3} E_{53.5}^{5/6} n_{-4}^{1/2} g_p^{-2/3} \mu\text{Jy} \sim 20 \mu\text{Jy}. \quad (7)$$

(ii) The X-ray flux density is about $20 \mu\text{Jy}$ at $t \sim 100\text{s}$, which indicates

$$F_{\text{XRT}}(t = 100\text{s}) \simeq F_{\text{max}}^f \left(\frac{3000\text{eV}}{\nu_m^f} \right)^{-(p-1)/2} = 35.7 \epsilon_{ef,-0.4}^{p-1} \epsilon_{Bf,-4}^{(p+1)/4} E_{53.5}^{(p+3)/4} n_{-4}^{1/2} f_{e1}^{3.1} g_p^{p-1} \mu\text{Jy} \sim 20 \mu\text{Jy}. \quad (8)$$

Combining the above two equations (7) and (8), we can express the fraction of the magnetic field energy and the number density as

$$\epsilon_{Bf,-4} \sim 0.66 \epsilon_{ef,-0.4}^{-4} E_{53.5}^{-1} g_p^{-4} g_{e2}^{12}, \quad (9)$$

$$n_{-4} \sim 0.66 \epsilon_{ef,-0.4}^4 E_{53.5}^{-1} g_p^4 g_{e2}^{-8.0} \quad (10)$$

where $g_{e1} = e^{p-2.5}$ and $g_{e2} = e^{(p-2.5)/(3p-1)}$ and we can naturally get $\epsilon_{ef} > 0.04 E_{53.5}^{-1/4} g_{e2}^3 g_p^{-1}$ from the condition $\epsilon_{Bf} < 1$.

Inserting equations (9) and (10) into equation (3), the downstream magnetic field strength is thus constrained to be

$$B' \sim 10 \epsilon_{ef,-0.4}^{-1/2} E_{53.5}^{-3/4} t_2^{-3/8} g_p^{-1/2} g_{e2}^{3.0} \text{mG}. \quad (11)$$

If the shocks involve a magnetic field amplification factor $f_B \geq 1$ (in addition to shock compression), the upstream magnetic field strength would be

$$B_u = B' / (4\Gamma f_B) \sim 7 f_B^{-1} E_{53.5}^{-1} g_{e2}^{2.0} \mu\text{G}. \quad (12)$$

Thus, the upstream magnetic field strength could be $\lesssim 5 - 10\mu\text{G}$ (e.g., Kumar & Barniol Duran 2010), apparently compatible with shock-compression of the typical magnetic field in the interstellar medium, with no need of magnetic field amplification. However, as we discuss in §6, the external density deduced here is much below the average interstellar value, and likely so would be the external magnetic field, so that additional field amplification may be needed.

Inserting equations (9) and (10) into equations (4), (5) and (6), the characteristic energies and the peak flux density of synchrotron emission are therefore

$$h\nu_c^f \sim 6.6 \times 10^9 \epsilon_{\text{ef},-0.4}^2 E_{53.5}^2 t_2^{-1/2} [1 + Y(\gamma_c^f)]^{-2} g_p^2 g_{e2}^{-10} \text{eV}, \quad (13)$$

$$h\nu_m^f \sim 4.0 \times 10^2 t_2^{-3/2} g_{e2}^{6.0} \text{eV}, \quad (14)$$

and

$$F_{\text{max}}^f \sim 90 g_{e2}^{2.0} \mu\text{Jy}, \quad (15)$$

respectively. The above equations show that $\nu_{\text{opt}} < \nu_m^f$ until $t \sim 1.4\text{ks}$, and $\nu_m^f < \nu_X < \nu_c$ under the constraint $\epsilon_{\text{ef},-0.4} E_{53.5} > 1.2 \times 10^{-3} t_2^{1/4} g_p^{-1} g_{e2}^{5.0}$, which is easy to satisfy, where $Y(\gamma_c^f) \ll 1$ as discussed in §2.2. Thus, they are consistent with our previous assumptions. The radiative efficiency in the assumed slow cooling regime is (Sari & Esin 2001)

$$\eta_r = \epsilon_{\text{ef}} \left(\frac{\nu_m^f}{\nu_c^f} \right)^{\frac{p-2}{2}} = 6.3 \times 10^{-3} \epsilon_{\text{ef},-0.4}^{3-p} E_{53.5}^{2-p} t_2^{-(p-2)/2} g_p^{2-p} g_{e1}^{-8.3} g_{e2}^{8.0(p-2)}, \quad (16)$$

which is much less than unity, consistent with our previous assumption of an adiabatic forward shock model.

In order to check whether the LAT emission predicted by synchrotron emission from an adiabatic forward shock can explain the LAT observations we need to study two situations.

(i) Under the condition $\epsilon_{\text{ef},-0.4} E_{53.5} > 0.39 g_p^{-1} g_{e2}^{5.0}$, we yield $\nu_m^f < 1\text{GeV} < \nu_c^f$ at $t \lesssim 100\text{s}$, the average synchrotron flux density from the forward shock in the LAT band (100MeV to 4GeV) is

$$F_{\text{LAT}}^f \sim F_{\text{max}}^f \left(\frac{1\text{GeV}}{h\nu_m^f} \right)^{-\frac{p-1}{2}} \sim 1.4 \times 10^{-3} t_2^{-3(p-1)/4} g_{e1}^{-6.4} \mu\text{Jy}. \quad (17)$$

which is independent of the electron energy $\epsilon_{\text{ef}} E$. In addition, the slope of the LAT light curve is also constrained, as $\alpha_{\text{LAT}} = 3(p-1)/4$, the same as that of the X-ray light curve. For $p = 2.5$, $\nu_m^f < 1\text{GeV} < \nu_c^f$ at $t \lesssim 100\text{s}$ is satisfied if $\epsilon_{\text{ef},-0.4} E_{53.5} > 0.39$, then the predicted LAT flux is $1.4 \times 10^{-3} \mu\text{Jy}$ at 100 s, consistent with the observational data within the error bars at around 100 s. The corresponding slope of the predicted LAT light curve is around -1.125 , which can explain the late-time data of the LAT observation. If we

take a small electron index, for example, $p \sim 2.2$, we have $\nu_m^f < 1\text{GeV} < \nu_c^f$ at $t = 100\text{s}$ if $\epsilon_{ef,-0.4}E_{53.5} > 0.60$. Then the predicted LAT flux can be calculated by equation (17), approximated as $\sim 8.9 \times 10^{-3} \mu\text{Jy}$ at 100 s, which is almost one order of magnitude smaller than the observed LAT flux. What's more, the slope of the predicted LAT light curve is about -0.9 , which is too shallow to explain the late-time LAT observation. Thus, in the case $\nu_m^f < 1\text{GeV} < \nu_c^f$ at 100 s, we can exclude the $p = 2.2$ model.

(ii) If the electron energy satisfies the condition $\epsilon_{ef,-0.4}E_{53.5} \leq 0.12g_p^{-1}g_{e2}^5$, the lower end of the LAT band, 100 MeV, is above the frequency ν_c^f , and the predicted LAT flux at $t = 100\text{s}$ can be calculated as

$$F_{\text{LAT}}^f \sim F_{\text{max}}^f \left(\frac{h\nu_c^f}{h\nu_m^f} \right)^{-\frac{p-1}{2}} \left(\frac{1\text{GeV}}{h\nu_c^f} \right)^{-\frac{p}{2}} \sim 3.6 \times 10^{-3} \epsilon_{ef,-0.4} E_{53.5} t_2^{-(3p-2)/4} g_p g_{e1}^{-7.4} g_{e2}^{3p-6} \mu\text{Jy}. \quad (18)$$

Inserting the condition $\epsilon_{ef,-0.4}E_{53.5} \leq 0.12g_p^{-1}g_{e2}^5$ into equation (18), we see that $F_{\text{LAT}}^f \leq 4.3 \times 10^{-4} g_{e1}^{-8.4} t_2^{-(3p-2)/4} \mu\text{Jy}$. For $p = 2.5$, the predicted LAT flux at 100 s is $F_{\text{LAT}}^f(100\text{s}) \leq 4.3 \times 10^{-4} \mu\text{Jy}$, which is almost one order of magnitude lower than the observed LAT flux. Thus in the case $\nu_{\text{LAT}} > \nu_c^f$ at 100 s, we can exclude the $p = 2.5$ model.

For $p = 2.2$, to be consistent with the observed LAT flux at 100 s, the condition $\epsilon_{ef,-0.4}E_{53.5} = 6.3 \times 10^{-2}$ is required, constraining the electron energy to a very small value. Here we adopt fairly standard values of $\epsilon_{ef} = 0.16 - 0.6$, similar to those observed in long GRBs, since these are determined by collisionless shock physics processes on microphysical scales, which should be independent of the global properties of GRBs. Then the constrained total kinetic energy could be $(0.13 - 0.47) \times 10^{53}\text{erg}$. Since the isotropic energy at 10keV – 30GeV energy band during $T_0 + 0.03\text{s} - T_0 + 0.53\text{s}$ is $E_{\text{iso}} = (1.08 \pm 0.06) \times 10^{53}\text{erg}$ (Ackermann et al. 2010b), the radiative efficiency of the prompt emission is in the range 70% – 89%. Moreover, we constrain $\epsilon_{Bf,-4} = 88\epsilon_{e,-0.4}^{-3}$ and $n_{-4} = 1.0\epsilon_{e,-0.4}^5$ by inserting the constraint $\epsilon_{ef,-0.4}E_{53.5} = 6.3 \times 10^{-2}$ into equations (9) and (10). The constrained ν_c^f is $h\nu_c^f = 1.1 \times 10^7\text{eV}$ at 100s, and $\nu_c^f < 10^8\text{eV}$ when $t > 1.2\text{s}$. Since the expected slope of the LAT light curve is $\alpha_{\text{LAT}} = (3p - 2)/4 = 1.15$ for $p = 2.2$ in the $\nu_{\text{LAT}} > \nu_c^f$ case, similar to that expected from the $p = 2.5$ model in the $\nu_m^f < \nu_{\text{LAT}} < \nu_c^f$ case, this can also explain the slope of the late-time LAT light curve. Even though ν_m^f decreases by a factor of 1.5 by taking $p = 2.2$ rather than taking $p = 2.5$, it doesn't change the optical break time by much, and we may not rule out the $p = 2.2$ model in the $\nu_{\text{LAT}} > \nu_c^f$ case.

Thus, both the $p = 2.5$ model in the $\nu_m^f < 1\text{GeV} < \nu_c^f$ case and the $p = 2.2$ model in the $\nu_{\text{LAT}} > \nu_c^f$ case can explain the late-time LAT light curve, leading to the same conclusion, since the predicted LAT light curves have the similar slope. For presentation purposes, hereafter, we discuss the $p = 2.5$ model in the $\nu_m^f < 1\text{GeV} < \nu_c^f$ case.

2.2. Impact of Klein-Nishina effects on the constraints

Wang et al. (2010) have studied the Klein-Nishina (KN) effects on high-energy gamma-ray emission in the early afterglow, and find that at early times the KN suppression on the IC scattering cross section for the electrons that produce the high-energy emission is usually strong, and therefore their inverse-Compton losses are small, with a Compton parameter Y of less than a few for a wide range of parameter space. This leads to a relatively bright synchrotron afterglow emission at high energies at early times. However, as the KN effects weaken with time, the inverse-Compton losses increase and the synchrotron high energy emission is increasingly suppressed, which leads to a more rapid decaying synchrotron emission. This provides a potential mechanism for the steep decay of the high-energy gamma-ray emission seen in some Fermi LAT GRBs.

The Compton parameter for electrons with Lorentz factor γ_e is defined as the ratio of the synchrotron self-inverse Compton (SSC) to the synchrotron emissivity, i.e.

$$Y(\gamma_e) \equiv \frac{P_{\text{SSC}}(\gamma_e)}{P_{\text{syn}}(\gamma_e)}. \quad (19)$$

When the KN suppression on the scattering cross section is negligible, $Y(\gamma_e) = Y(\gamma_c)$ is a constant for the slow-cooling case (Sari & Esin 2001). However, for high energy electrons with a significant KN effect, $Y(\gamma_e)$ is no longer a constant and this affects the electron radiative cooling function, as well as the continuity equation of the electron distribution. The self-consistent electron distribution is given by

$$N(\gamma_e) = \begin{cases} C_1 \gamma_e^{-p} & \gamma_m < \gamma_e < \gamma_c \\ \frac{1+Y(\gamma_e)}{1+Y(\gamma_c)} C_1 \gamma_c \gamma_e^{-p-1} & \gamma_c < \gamma_e \end{cases} \quad (20)$$

for the slow-cooling case (Nakar et al. 2009; Wang et al. 2010), where C_1 is a constant. The high energy synchrotron photons with energy $h\nu_*$ are produced by electrons with Lorentz factor γ_* which typically have $\gamma_* > \max(\gamma_c, \gamma_m)$. Thus, the number density of electrons of γ_* is

$$N(\gamma_*) = \frac{1 + Y(\gamma_c)}{1 + Y(\gamma_*)} C_1 \gamma_c \gamma_*^{-p-1} = \frac{N_{\text{syn}}(\gamma_*)}{1 + Y(\gamma_*)}, \quad (21)$$

where $N_{\text{syn}}(\gamma_*) = C_1 \gamma_c [1 + Y(\gamma_c)] \gamma_*^{-p-1}$ is the number density of electrons of γ_* when only the synchrotron cooling is considered (Sari et al. 1998). Therefore, the number density of electrons with Lorentz factor γ_* is a factor of $1 + Y(\gamma_*)$ lower than that in the case where only the synchrotron cooling is considered. Thus the synchrotron luminosity is correspondingly reduced by the same factor. We have $Y(\gamma_*) \propto t^{1/2}$, in the slow cooling regime, as long as $\gamma_* > \Gamma m_e c^2 / h\nu_m^f$ (Wang et al. 2010). In that case, if $Y(\gamma_*) \gg 1$ the synchrotron luminosity is

suppressed by the factor $Y(\gamma_*)$ which is in proportion to $t^{1/2}$, i.e. the light curve decay of the high energy synchrotron emission could be steepened by a factor 1/2 at most. Meanwhile, the distribution of electrons which are in the region $\gamma_m < \gamma < \gamma_c$ is not affected by $Y(\gamma)$, due to equation 20, thus the lower energy synchrotron emission decay slope is normal.

The critical photon energy above which the scattering with electrons of energy γ_e just enters the KN scattering regime is defined as $h\nu_{\text{KN}}(\gamma_e) \equiv \Gamma m_e c^2 / \gamma_e$, i.e.

$$h\nu_{\text{KN}}(\gamma_c^f) = \Gamma m_e c^2 / \gamma_c^f = 0.52 \epsilon_{\text{ef},-0.4}^{-2} E_{53.5}^{-1} t_2^{-1/2} g_p^{-2} g_{e2}^{8.0} [1 + Y(\gamma_c^f)] \text{eV}. \quad (22)$$

which is much smaller than ν_m^f under the condition $\epsilon_{\text{ef},-0.4}^2 E_{53.5} > 0.13 t_4 g_p^{-2} g_{e2}^{2.0} [1 + Y(\gamma_c^f)]$. In this case the synchrotron-self Compton scattering is strongly suppressed due to KN effects, and

$$\begin{aligned} Y(\gamma_c^f) [1 + Y(\gamma_c^f)] &= \frac{\epsilon_{\text{ef}}}{\epsilon_{\text{Bf}}} \left(\frac{\gamma_c^f}{\gamma_m^f} \right)^{2-p} \left(\frac{\nu_m^f}{\nu_c^f} \right)^{(3-p)/2} \left(\frac{\nu_{\text{KN}}(\gamma_c^f)}{\nu_m^f} \right)^{4/3} \\ &= 1.4 \times 10^{-4} [1 + Y(\gamma_c^f)]^{7/3} \epsilon_{\text{ef},-0.4}^{4/3} E_{53.5}^{-4/3} t_2^{5/6} g_p^{1/3} g_{e2}^{-1.3}. \end{aligned} \quad (23)$$

From the above equation, we find that $Y(\gamma_c^f) \ll 1$ under the condition $\epsilon_{\text{ef},-0.4}^{-1} E_{53.5} \gg 0.023 t_4^{5/8} g_p^{1/4} g_{e2}^{-0.98}$, which is easy to be satisfied before $t < 10^4$ s. Therefore, since $Y(\gamma_*) \leq Y(\gamma_c) \ll 1$, the distribution of electrons which contribute to the high-energy synchrotron photons doesn't change, according to equation (20), which means that the decay slope of synchrotron high energy emission can not be affected by $Y(\gamma_*)$.

3. Forward Shock Synchrotron Emission Evolution

We adopt the following parameters for the calculations. From equation (17), we see that the flux density in the LAT range is independent of the total isotropic kinetic energy and the electron energy fraction at $t < 100$ s, under the constraint $\epsilon_{\text{ef},-0.4} E_{53.5} > 0.39$. Thus, we can fix the total energy of the afterglow as $E = 3.0 \times 10^{53}$ erg, indicating a radiation efficiency as 25%. Even if we choose other values of the total kinetic energy under the constraint $\epsilon_{\text{ef},-0.4} E_{53.5} > 0.39$, our conclusion will not change. Then the fraction of electron energy is constrained as $\epsilon_{\text{ef}} > 0.16$. We adopt fairly standard values of $\epsilon_{\text{ef}} \geq 0.16$. From the equations (9) and (10), we can get the values of $\epsilon_{\text{Bf}} = 2.6 \times 10^{-3} - 1.3 \times 10^{-5}$, corresponding to an external density range [$n = 1.7 \times 10^{-6} \text{cm}^{-3} - 3.3 \times 10^{-4} \text{cm}^{-3}$]. These densities range from much less than the intergalactic medium (IGM), up to a low density inter-cluster medium (ICM) or possibly galactic halo baryon density. The critical Lorentz factor which is the boundary between the thin and thick shell cases (Kobayashi et al. 2007) is $\Gamma_c = [3(1+z)^3 E / 32\pi n m_p c^5 T^3]^{1/8} \sim 5.2 \times 10^3 E_{53.5}^{1/8} n_{-4}^{-1/8} T_{-0.5}^{-3/8}$, where the duration of GRB 090510

is $T = 0.30 \pm 0.07$ s. For an initial Lorentz factor which is not too large, it is reasonable to assume that the initial Lorentz factor is smaller than the critical Lorentz factor, which means the shell has given the ambient medium an energy comparable to its initial energy at the deceleration time $t_{\text{dec}} = [3(1+z)^3 E / 32\pi c^5 n m_p \Gamma_0]^{1/3} > T$, indicating the thin shell case. Then the initial Lorentz factor of the forward shock can be expressed as a function of the deceleration time, which is $\Gamma_0 = 3.3 \times 10^3 E_{53.5}^{1/8} n_{-4}^{-1/8} t_{\text{dec}}^{-3/8}$. If, for example, we take an initial Lorentz factor as suggested by previous Fermi analyses of $2.2 \times 10^3 - 5.2 \times 10^3$, and a not too small number density of $n \sim 10^{-4} \text{cm}^{-3}$, we would obtain a deceleration time of $t_{\text{dec}} \sim 0.3\text{s} - 3\text{s}$.

To calculate the dynamics of the evolution of the blast wave including the transition from the quasi-free expansion, through the deceleration and into the self-similar phase, we use the relativistic hydrodynamics equations for the evolution of the shock radius R , the mass m swept up by the shock, the opening half-angle of jet θ and the Lorentz factor of the shock Γ (e.g., Huang et al. 2000b) (see Appendix A), and solve these equations numerically. The solution of these equations provides the dynamical quantities which we use to calculate the radiation spectrum and the light curves discussed in the following. We take into account also the jet evolution as it goes through the jet break and starts to expand sideways. The half-angle of the jet evolves as $d\theta_j = (c_s dt' / r) = [(1 + \beta)\Gamma c_s / r] dt$, with a spreading velocity in the comoving frame approximated by the sound speed c_s (Rhoads 1997, 1999; Huang et al. 2000a). After the inverse Lorentz factor becomes larger than the initial jet angle, the spreading of the jet speeds up the shock deceleration significantly, which leads to a steeper light curve.

In figures 1 and 2 we present model light curves in the LAT, XRT and UVOT bands for two choices of parameters. The forward shock light curves (solid black lines) are shown, for each density choice, for two different Lorentz factors and jet opening angles. A smaller opening angle is chosen for a larger Lorentz factor in order to get a certain jet break time.

In figure 1, we show a solution with a density of $n = 1 \times 10^{-6} \text{cm}^{-3}$, which would correspond to a sub-average density IGM environment. Under the assumptions $\nu_{\text{opt}} < \nu_{\text{m}}^{\text{f}}$ before the optical break time and $\nu_{\text{m}}^{\text{f}} < \nu_{\text{X}} < \nu_{\text{c}}^{\text{f}}$, the steep decay of the latter parts of the X-ray and optical light curves can be explained using such a forward shock synchrotron emission going through a jet spreading phase, as shown in figure 1 and 2. Note, however, that, as in other analyses too, the late-time optical data are challenging to fit. This leads to a model forward shock light curve and spectral fit to the X-ray and optical observations satisfying all the constraints of §2.1, for a set of parameters $\epsilon_{\text{ef}} = 0.17$, $E = 3 \times 10^{53} \text{erg}$, $p = 2.5$, $\epsilon_{\text{Bf}} = 7.0 \times 10^{-3}$, and $\theta_0 = 0.45^\circ$ for $\Gamma_0 = 4500$, or $\theta_0 = 0.38^\circ$ for $\Gamma_0 = 9000$. The collimation corrected energies are 4.6×10^{48} and 3.3×10^{48} erg.

In figure 2 we show the forward shock solutions for a more moderate density of $n = 10^{-3}\text{cm}^{-3}$, corresponding to a galactic halo or interarm medium, which satisfy the low energy constraints as well as the afterglow epoch LAT, XRT and UVOT data points. The parameters are $\epsilon_{ef} = 0.6$, $\epsilon_{Bf} = 1 \times 10^{-5}$, $p = 2.5$ and $E = 3 \times 10^{53}$ erg, for a choice of $\theta_0 = 1.3^\circ$ and $\Gamma_0 = 1900$, and also for a choice of $\theta_0 = 1.1^\circ$ and $\Gamma_0 = 3800$. The collimation corrected energies are 3.9×10^{49} and 2.8×10^{49} erg, which is a typical energy for a short GRB. Despite the larger ϵ_{ef} in this fit, the forward shock is still in the adiabatic regime according to equation (16).

In Figures 1 and 2 the LAT energy band light curves predicted by the forward shock synchrotron model shown in black solid lines (thicker for the larger Lorentz factor and smaller opening angle choice, thinner for the smaller Lorentz factor and larger angle choice). These appear to explain well the late time LAT emission, i.e. after 3 seconds, either with the larger or smaller angle/Lorentz factor, no matter how small the deceleration time is, but they fall below the first six LAT data points. This difference between the early time observed LAT data and the synchrotron forward shock emission suggests that there may be another radiation component (whose contribution can be represented by the gray dotted lines in Figures 1 and 2, corresponding to the high latitude emission of the prompt emission with variability timescale $\Delta t = 0.5\text{s}$), in addition to the forward synchrotron contribution (shown as the black solid lines), at least for its decaying portion. The gray solid lines are the sum of the steep decay component and the forward synchrotron emission with a larger Lorentz factor (the first, lower data point could be part of either a rising portion or a variable portion of the gray dotted component). Thus, it is possible that the early-time high-energy emission is not from the afterglow forward shock synchrotron emission, instead having a different origin. In the next section we discuss possible origins for the first six data points in the LAT band around the deceleration time.

4. Other Possible Components around the Deceleration Time

Besides the forward shock synchrotron emission, around the deceleration time there are several other possible emission components which could contribute to the early LAT observations. Their importance can be estimated using approximate values for the characteristic quantities at the deceleration time. At the deceleration time, the Blandford-McKee self-similar solution is not yet applicable. For this we can take the usual value of the energy as $E = \frac{4\pi}{3} R^3 \Gamma^2 n m_p c^2$ and $R = 2\Gamma^2 ct / (1+z)$ as the radius at the deceleration time (Sari et al. 1998), from which we obtain the initial Lorentz factor of the shock and the deceleration

radius, which are

$$\Gamma_0 = 3.3 \times 10^3 E_{53.5}^{1/8} n_{-4}^{-1/8} t_{\text{dec}}^{-3/8} \quad (24)$$

$$R_{\text{dec}} = 3.5 \times 10^{17} E_{53.5}^{1/4} n_{-4}^{-1/4} t_{\text{dec}}^{1/4} \text{cm}. \quad (25)$$

Before we examine the other possible components around the deceleration time, we confirm that the forward shock synchrotron emission cannot explain the observation at early times in more details. We can then estimate the approximate high energy emission at the deceleration time under the previous constraints provided by the low energy observations. Here we take the Lorentz factor and radius at the deceleration time as $\Gamma_d \sim \Gamma_0/\sqrt{2}$ and $R_d \sim R_{\text{dec}}/\sqrt{2}$, which are close to the values indicated by the numerical evolution of the previous section. Inserting the above Γ_d and R_d into the first expressions of equations (1) – (6), and meanwhile adopting equations (9) and (10), the characteristic frequencies and peak flux density of the forward shock synchrotron emission at the deceleration time are then

$$h\nu_{\text{m,d}}^f \sim 6.8 \times 10^5 t_{\text{dec}}^{-3/2} g_{e2}^{6.0} \text{eV}, \quad (26)$$

$$h\nu_{\text{c,d}}^f \sim 3.9 \times 10^{10} \epsilon_{\text{ef},-0.4}^2 E_{53.5}^2 t_{\text{dec}}^{-1/2} g_p^2 g_{e2}^{-10} \text{eV}, \quad (27)$$

$$F_{\text{max,d}}^f \sim 12 g_{e2}^{2.0} \mu\text{Jy}. \quad (28)$$

Ghisellini et al. (2010) suggests the radiative forward shock model to explain the steep temporal decay of high energy emission, which requires $\nu_{\text{m}}^f > \nu_{\text{c}}^f$ to get the fast cooling case. However, the radiative model cannot explain the shallower decay at later time ($t > 10\text{s}$) (as seen in Figure 7 in Ghisellini et al. (2010)), which agrees better with an adiabatic model in slow cooling case at that time. According to the constrained characteristic frequencies, the fast cooling case at the deceleration time requires that

$$\epsilon_{\text{ef}} < 1.7 \times 10^{-3} E_{53.5}^{-1} t_{\text{dec}}^{-1/2} g_p^{-1} g_{e2}^{8.0}, \quad (29)$$

which is inconsistent with their assumption of a very high energy fraction of electrons $\epsilon_{\text{ef}} = 0.9$. This is because Ghisellini et al. (2010) assume the late-time emission to be also in the fast cooling case, and do not take into account the constraints from the low energy emission.

In addition, using equations (9) and (10), we get an estimate for the forward shock synchrotron emission at 1GeV at the deceleration time,

$$F_{1\text{GeV,d}}^f = F_{\text{max,d}}^f \left(\frac{1\text{GeV}}{h\nu_{\text{m,d}}^f} \right)^{-\frac{p-1}{2}} \sim 0.049 t_{\text{dec}}^{-3(p-1)/4} g_{e1}^{-2.6} \mu\text{Jy}. \quad (30)$$

This is almost one order of magnitude below the observed LAT flux density, for the case when the deceleration time is smaller than 3s (this is seen also in Figures 1 and 2). The

synchrotron forward shock emission cannot explain the early-time high-energy emission (the first six LAT data points near the deceleration time), although it can explain very well the late LAT results (beyond the sixth LAT data point, when the afterglow can be considered as established), which are consistent with the numerical results in §3.

Thus, we find that there has to be another component, contributing to the early high energy emission. In the rest of this section we consider several such possibilities, such as a reverse shock synchrotron component, a reverse shock SSC component or a cross IC component (forward/reverse shock synchrotron photons scattered by electrons from reverse-shocked/forward-shocked region), a high latitude (curvature) component of the prompt high energy emission.

4.1. Reverse Shock Synchrotron Emission

We consider the thin shell case as is assumed in §3, the flux peaks at the crossing time of the reverse shock $t_{\times} = t_{\text{dec}} > T$ with Lorentz factor $\Gamma_{\times} = \Gamma_{\text{d}}$, and the ratio of the comoving number densities of the forward-shocked to that of the reverse-shocked regions is given by $n_{\text{r}}/n_{\text{f}} \sim \Gamma_{\text{d}} \sim 2.3 \times 10^3 E_{53.5}^{1/8} n_{-4}^{-1/8} t_{\text{dec}}^{-3/8}$ (Kobayashi et al. 2007). The internal energy densities e and the bulk Lorentz factors Γ of the two regions are equal with each other (Zhang et al. 2003). Consequently, we have that

$$\frac{\nu_{\text{m}}^{\text{r}}}{\nu_{\text{m}}^{\text{f}}} = \left(\frac{n_{\text{r}}}{n_{\text{f}}}\right)^{-2} \mathfrak{R}_B \mathfrak{R}_e^2, \quad \frac{\nu_{\text{c}}^{\text{r}}}{\nu_{\text{c}}^{\text{f}}} = \mathfrak{R}_B^{-3} [1 + Y(\gamma_{\text{c},\times}^{\text{r}})]^{-2}, \quad \frac{F_{\text{max}}^{\text{r}}}{F_{\text{max}}^{\text{f}}} = \frac{n_{\text{r}}}{n_{\text{f}}} \mathfrak{R}_B, \quad (31)$$

characterized by the ratios $\mathfrak{R}_B \equiv \left(\frac{\epsilon_{B\text{r}}}{\epsilon_{B\text{f}}}\right)^{\frac{1}{2}}$, $\mathfrak{R}_e \equiv \frac{\epsilon_{\text{er}}}{\epsilon_{\text{ef}}}$.

The minimum and cooling frequencies of the reverse shock synchrotron emission at the crossing time under the low energy constraints are

$$h\nu_{\text{m},\times}^{\text{r}} = 1.1 \epsilon_{\text{ef},-0.4} E_{53.5}^{-1/4} t_{\text{dec}}^{-3/4} \mathfrak{R}_{B,1} \mathfrak{R}_e^2 g_p g_e^{4.0} \text{eV}, \quad (32)$$

$$h\nu_{\text{c},\times}^{\text{r}} = 3.9 \times 10^7 \epsilon_{\text{ef},-0.4}^2 E_{53.5}^2 t_{\text{dec}}^{-1/2} \mathfrak{R}_{B,1}^{-3} g_p^2 g_e^{-10} [1 + Y(\gamma_{\text{c},\times}^{\text{r}})]^{-2} \text{eV}. \quad (33)$$

According to §2.2, we have $Y(\gamma_{\text{r}}^{\text{r}}) < Y(\gamma_{\text{c}}^{\text{r}}) \ll 1$ around the deceleration time, thus the synchrotron spectrum does not change and the ratio of the reverse shock synchrotron flux to forward shock synchrotron flux can be calculated as

$$\frac{F_{1\text{GeV},\times}^{\text{r}}}{F_{1\text{GeV},\times}^{\text{f}}} = \frac{F_{\text{max},\times}^{\text{r}}}{F_{\text{max},\times}^{\text{f}}} \left(\frac{\nu_{\text{m},\times}^{\text{r}}}{\nu_{\text{m},\times}^{\text{f}}}\right)^{\frac{p-1}{2}} \left(\frac{h\nu_{\text{c},\times}^{\text{r}}}{1\text{GeV}}\right)^{\frac{1}{2}} = \left(\frac{n_{\text{r}}}{n_{\text{f}}}\right)^{-p+2} \mathfrak{R}_e^{p-1} \mathfrak{R}_B^{(p+1)/2} \left(\frac{h\nu_{\text{c},\times}^{\text{r}}}{1\text{GeV}}\right)^{1/2}, \quad (34)$$

Inserting equations (9) and (10) into equation (34), the ratio turns to be

$$\frac{F_{1\text{GeV},\times}^{\text{r}}}{F_{1\text{GeV},\times}^{\text{f}}} = 0.23 \epsilon_{\text{ef},-0.4}^{p/2} E_{53.5}^{-p/4+3/2} t_{\text{dec}}^{3p/8-1} \mathfrak{R}_{B,1}^{p/2-1} \mathfrak{R}_{e,0}^{p-1} g_{e1}^{-6.7} g_p^{p/2} g_{e2}^{-p-3.0}. \quad (35)$$

The ratio could be as high as 0.59 since the total kinetic energy can be as high as $E \sim 9.0 \times 10^{53} \text{erg}$ by considering a reasonable radiation efficiency $\gtrsim 10\%$. Considering equation (30), the flux density from reverse shock synchrotron emission cannot be as high as $\sim \mu\text{Jy}$ to explain the observations at early times. Thus, the reverse shock synchrotron emission is unlikely to contribute to the early-time LAT observation.

4.2. The SSC and EIC Emission

Besides the reverse synchrotron emission, we consider the other four possible IC processes, including the synchrotron self-Compton (SSC) processes in forward and reverse shocks, and two combined-IC processes (i.e. scattering of reverse-shock synchrotron photons on electrons accelerated in forward shocks and forward-shock synchrotron photons on electrons accelerated in reverse shocks).

The optical depth of inverse Compton scattering in the reverse shock in the Thomson regime is $\tau^{\text{r}} = \frac{1}{3} \sigma_{\text{T}} n_{\text{r}} R_{\text{d}} / \Gamma_{\text{d}} = 7.7 \times 10^{-8} \epsilon_{\text{ef},-0.4}^{5/2} E_{53.5}^{-1/4} t_{\text{dec}}^{-1/8} g_p^{5/2} g_{e2}^{-5.0}$ (Wang et al. 2001). The optical depth to inverse Compton scattering in the forward shock in the Thomson regime is $\tau^{\text{f}} = \frac{1}{3} \sigma_{\text{T}} n_{\text{f}} R_{\text{d}} = 3.8 \times 10^{-12} \epsilon_{\text{ef},-0.4}^3 E_{53.5}^{-1/2} t_{\text{dec}}^{1/4} g_p^3 g_{e2}^{-6.0}$. Taking the peak flux of synchrotron emission at the crossing time of the reverse shock and forward shock, which are $F_{\text{max}}^{\text{r}} = 0.30 \epsilon_{\text{ef},-0.4}^{-1/2} E_{53.5}^{1/4} t_{\text{dec}}^{-3/8} \mathfrak{R}_{B,1} g_p^{-1/2} g_{e2}^{3.0} \text{Jy}$ and $F_{\text{max}}^{\text{f}} = 12 g_{e2}^{2.0} \mu\text{Jy}$, respectively, we can get the peak flux density of the four Inverse-Compton components as follows (Wang et al. 2001),

$$F_{\text{max}}^{\text{IC,rr}} = \tau^{\text{r}} F_{\text{max}}^{\text{r}} = 2.2 \times 10^{-8} \text{Jy} \epsilon_{\text{ef},-0.4}^2 t_{\text{dec}}^{-1/2} \mathfrak{R}_{B,1} g_p^2 g_{e2}^{-2.0}, \quad (36)$$

$$F_{\text{max}}^{\text{IC,rf}} = \tau^{\text{r}} F_{\text{max}}^{\text{f}} = 8.8 \times 10^{-13} \text{Jy} \epsilon_{\text{ef},-0.4}^{5/2} E_{53.5}^{-1/4} t_{\text{dec}}^{-1/8} g_p^{5/2} g_{e2}^{-3.0}, \quad (37)$$

$$F_{\text{max}}^{\text{IC,fr}} = \tau^{\text{f}} F_{\text{max}}^{\text{r}} = 1.1 \times 10^{-12} \text{Jy} \epsilon_{\text{ef},-0.4}^{5/2} E_{53.5}^{-1/4} t_{\text{dec}}^{-1/8} \mathfrak{R}_{B,1} g_p^{5/2} g_{e2}^{-3.0} \quad (38)$$

and

$$F_{\text{max}}^{\text{IC,ff}} = \tau^{\text{f}} F_{\text{max}}^{\text{f}} = 4.5 \times 10^{-17} \text{Jy} \epsilon_{\text{ef},-0.4}^3 E_{53.5}^{-1/2} t_{\text{dec}}^{1/4} g_p^3 g_{e2}^{-4.0}, \quad (39)$$

respectively, where the superscripts ‘rr’ and ‘ff’ mean the SSC emission in reverse shock and forward shock respectively, ‘fr’ and ‘rf’ mean the scattering of reverse shock photons on the electrons in forward shocks and forward shock photons on the electrons in reverse shocks. Therefore, the IC contributions (except for the SSC emission in the reverse shock) can be excluded, since even their peak fluxes are much smaller than the early-time LAT

observations. Although the peak flux of the SSC emission in the reverse shock is close to the observed flux, the reverse shock SSC emission can also be excluded because its flux peaks at a low energy of about 20keV, indicating that the flux in the LAT band is about 6 orders lower than the peak flux. A low flux for these IC processes is mainly due to a very low circum-burst density in GRB 090510 inferred from the low-energy observations.

4.3. The High Latitude Prompt Emission

The spectrum of GRB 090510 shows a power-law component in the LAT band ($> 100\text{MeV}$), whose physical origin at early times is unclear. One might consider the early part of the extended emission (shown by the gray dotted line with a decay slope $\alpha_{\text{Lat}}(0.37-3\text{s}) = 2.0$ in Figures 1 and 2) is due to the high-latitude emission of the prompt emission (Kumar & Panaitescu 2000). Because photons from high latitude regions with respect to the line of sight will arrive later than that from low latitude region due to the curved front surface of the jet, one observes a fast decreasing emission rather than an abrupt stop of the emission, the so-called ‘‘curvature effect’’. Then the high latitude emission flux of the prompt emission evolves as

$$F_{\nu}(t) \propto \left[\frac{t - (t_0 - \Delta t)}{\Delta t} \right]^{-2-\beta} \quad (40)$$

according to Toma et al. (2009)(The details are shown in Appendix B), where t_0 is the pulse peak time. According to Ackermann et al. (2010b) and Abdo et al. (2009b), the variability timescale derived from the BGO emission (100keV–few MeV) is about $14 \pm 2\text{ms}$ in the time interval $0.17 - 0.37\text{s}$ since the BAT trigger, but the variability timescale for the LAT emission is not determined. If we assume that the variability timescale for the high energy (larger than 100MeV) emission, which is dominated by the power law component, is the same as that of BGO observation, then we adopt $\Delta t \sim 0.01\text{s}$ in equation (40). Thus, the high latitude flux of the prompt emission at $t_0 + 0.1\text{s}$ is $F(t_0 + 0.1\text{s}) = 11^{-2-\beta}F(t_0)$. Since the index of the power law component in the time interval $0.17 - 0.37\text{s}$ is 1.66 ± 0.04 (Ackermann et al. 2010b; Abdo et al. 2009b), we take the rough value $\beta \sim 0.66$. Then the flux of the high-latitude emission at $t_0 + 0.1\text{s}$ will be reduced by a factor of ~ 600 relative to that of the line-of-sight emission at $t_0 \sim 0.37$, which is too steep to explain the early high energy emission at $t = 0.37 - 3\text{s}$.

Since the origin of the LAT emission in the prompt phase, dominated by the extra power-law component, is unclear and can be different from that of the Band component in the GBM energy range, the variability timescale in the LAT range can generally be different from $\Delta t \sim 0.01\text{s}$. In particular, the emission radius of the extra high energy component may be much larger than that of the Band component, which may lead to a much larger pulse

width in the LAT energy range than in the GBM energy range (see e.g., Toma et al. (2010)). If we take $\Delta t \sim 0.5\text{s}$, then the high latitude flux of the prompt emission at $t_0 \sim 0.37\text{s}$ evolves as $F(t) \sim (2t + 0.26\text{s})^{-2.66} F(0.37\text{s})$, which together with the synchrotron forward shock emission with a deceleration time $t_{\text{dec}} \leq (2 - 3)\text{s}$ can explain the early high energy emission at $t \sim 0.37 - 3\text{s}$, shown in Fig 1.

5. The Line-of-Sight Prompt Emission as the Origin of the Early-Time Afterglow High-Energy Emission

As a final possibility, we consider the possible influence of the tail-end of the prompt emission in the description of the early afterglow. In §3 and §4 we assumed a small GRB duration $T_{90} = 0.30 \pm 0.07\text{s}$, following De Pasquale et al. (2010) based on the observations in the GBM and BAT bands. Under this assumption, we discussed the forward shock synchrotron emission, the forward reverse shock synchrotron emission, the four possible crossed inverse Compton processes, and the high latitude emission of the prompt emission, and we concluded that none of them can explain the early decaying part of the high energy emission at $0.3 \lesssim t \lesssim 3\text{s}$ except for the high latitude portion of the prompt emission with a larger variability time scale plus the synchrotron forward shock emission with a deceleration time $t_{\text{dec}} \leq (2 - 3)\text{s}$.

We focus on the BAT detections around $T_0 + (1 - 3)\text{s}$, shown in De Pasquale et al. (2010), which implies that the prompt emission could last until such times. We calculate the flux of the synchrotron forward shock emission at $t = 3\text{s}$ for $p = 2.5$ in the BAT energy range, and obtain $\sim 52\mu\text{Jy}$ (the flux is similar for $p = 2.2$). This is about one order of magnitude smaller than the observed flux. Thus these BAT detections are not from the external shock, but may be attributed to the prompt emission.

The LAT prompt emission may also last until such times. Ackermann et al. (2010b) obtain no significant temporal correlation between NaI (8keV – 260keV) data and the LAT data $> 100\text{MeV}$ between $t = 0.17\text{s}$ and $t = 0.47\text{s}$. This does not necessarily indicate that the LAT prompt emission (the extra component) and the GBM prompt emission (Band component) have fully unrelated origins. Some theoretical models suggest that the two components may arise at different radii (e.g., Toma et al. (2010), Wang et al. (2006)) in the same shells, or the two components may arise by the leptonic and hadronic processes in the same internal shock (e.g., Asano et al. (2009); Razzaque (2010)). Therefore it appears reasonable to consider that GRB 090510 has a duration as long as $2 - 3\text{s}$ and the high energy emission before $t \sim 2 - 3\text{s}$ is a part of the prompt emission.

Under this new assumption, with a longer GRB duration $T \sim 2.0\text{s}$, one infers a critical Lorentz factor $\Gamma_c \sim 2.0 \times 10^3 E_{53.5}^{1/8} n_{-3}^{-1/8} T_{0.3}^{-3/8}$. For the thin shell case with an initial Lorentz factor Γ_0 smaller than Γ_c , the shell will be decelerated efficiently by the reverse shock after the GRB main duration. The high energy light curve with the initial Lorentz factor $\Gamma_0 = 1900$ and the number density $n = 10^{-3}\text{cm}^{-3}$ is shown by the thin solid line in Figure 2, which can explain the late-time high energy emission well. If we assume that the LAT emission around $t = 2\text{s}$ is a flare of duration $\Delta t = 1\text{s}$, which peaks at $t_0 = 2\text{s}$ with a peak flux $F(t_0)$, and having (De Pasquale et al. 2010) a spectral index $\beta = 0.41_{-0.31}^{+0.28}$ at $t = 1.5 - 2.5\text{s}$, then the flux due to curvature effect at $t = 3.5\text{s}$ is $F(t) = 0.11F(t_0)$, which is compatible with the seventh data point. In this case, the deceleration time could in principle be even larger, implying a smaller Lorentz factor, but due to the lack of precise information about the last flare, e.g., its duration and the flux peak time, we cannot use this to derive a firmer deceleration time.

For a larger initial Lorentz factor $\Gamma_0 > \Gamma_c$, the reverse shock will transition from the Newtonian phase to the relativistic phase at the time $t_N = (E/16\pi\Delta nm_p c^4 \Gamma_0^8)^{1/2} = 0.081 E_{53.5}^{1/2} \Gamma_{0,3.7}^{-4} n_{-4}^{-1/2} \text{s}$ (Sari 1997), with the width of the shell in the comoving frame $\Delta = cT/(1+z) = 3.1 \times 10^{10} T_{0.3} \text{cm}$. The deceleration time when the dissipated energy is comparable to the total kinetic energy of the shell is about $t_{\text{dec}} = 2T$. At the time $t_N < t < t_{\text{dec}}$, the Lorentz factor of the forward shock evolves as $\Gamma \propto t^{-1/4}$, and the radius of the shell evolves as $R \propto t^{1/2}$. Thus, the characteristic frequencies and the peak flux density evolve as $\nu_{\text{min}}^r \propto t^{-1}$, $\nu_c^r \propto t^{-1}$ and $F_{\text{max}} \propto t$. As a result, the flux of high energy emission in the region $\nu_m^f < \nu_{\text{LAT}} < \nu_c^f$ evolves as $F_{\text{LAT}} \propto t^{(-p+3)/2}$; and the flux density of high energy emission in the region $\nu_{\text{LAT}} > \nu_c^f$ evolves as $F_{\text{LAT}} \propto t^{(-p+2)/2}$. This shows that the forward shock synchrotron emission in the thick shell case cannot explain the early-time high energy emission due to its flatter light curve. And the reverse shock emission in the thick shell case can also be excluded, using similar calculations as in §4.

Based on the above analysis, while the forward shock synchrotron afterglow dominates the LAT emission at late times, the early times LAT emission must be attributed to a prompt emission, which can be limited from above by a high-latitude curvature emission envelope.

6. Discussion and Conclusions

We have investigated whether the photons received by the LAT can be explained solely by the forward shock afterglow emission or whether the prompt emission necessarily contributes to the early part of this emission. We have addressed this question with the help of the broad-band observations from the XRT and UVOT instruments onboard of Swift and the LAT onboard of Fermi for the case of the short GRB 090510, obtaining constraints on

the extended high-energy emission based on the XRT and UVOT observations.

We have obtained a good fit to the XRT and UVOT observations (except for the late-time optical data) in terms of synchrotron emission from an adiabatic forward shock in spreading jet model, which constrains the environment of this short burst, implying a low number density $n \sim 10^{-3} - 10^{-6} \text{cm}^{-3}$, consistent with a binary progenitor scenario (e.g., Belczynski et al. 2006), corresponding to an electron energy fraction $\epsilon_{ef} \sim 0.6 - 0.2$ and a weak magnetic field with an energy fraction $\epsilon_{Bf} \sim 10^{-5} - 10^{-2}$. The latter could in principle be due to an upstream magnetic field of $\sim 7 \mu\text{G}$ just shock-compressed, without need for magnetic field amplification (Kumar & Barniol Duran 2010). However, the magnetic field values of $\sim \mu\text{G}$ derived in our galaxy correspond to an average ISM of density $n \sim 1 \text{cm}^{-3}$, whereas the fits for GRB 090510 indicate external densities comparable to a halo or intergalactic medium with $n \sim 10^{-3} - 10^{-6} \text{cm}^{-3}$, where based on flux-freezing the field would be expected to be much less than μG . Thus, the magnetic field may still need to be amplified in the shock. We note also that while the electron energy fraction can be as high as 0.6, the adiabatic condition is still satisfied, since the low energy emission constrains the radiation to be in the slow cooling case, indicating a radiation efficiency much smaller than unity, in contrast to the radiative regime assumption of Ghisellini et al. (2010), where they did not take into account low energy constraints.

In De Pasquale et al. (2010), it is assumed that the LAT data at $t = 1 - 200\text{s}$ with slope -1.38 arises from synchrotron emission in the regime $\nu_{\text{LAT}} > \nu_c^f$, i.e., $\nu_c < 10^8 \text{eV}$, in contrast to our conclusion that the synchrotron emission in the regime $\nu_c^f > 1 \text{GeV}$ evolving with slope ~ -1.1 . Part of the difference may be due to De Pasquale et al. (2010) using the formulae of Granot & Sari (2002), while we used the formulae of Sari et al. (1998). However, applying the constraints on $\epsilon_B, n, \epsilon_{ef}E$ in De Pasquale et al. (2010) and taking $p = 2.5$ in the expression for ν_c^f from Granot & Sari (2002), one obtains $\nu_c^f \simeq 6.3 \times 10^7 \text{eV}$ at 100s . Therefore, $\nu_c^f = 6.3 \times 10^8 \text{eV}$ at 1s since $\nu_c \propto t^{-1/2}$, falling in the LAT band, inconsistent with the De Pasquale et al. (2010) assumption. The simple power-law decay shown in their Figure 1 is not applicable due to the ν_c crossing through the LAT band, and it overestimates the LAT photon flux by a factor of 1.7 at $t = 1\text{s}$ and 2.1 at $t \sim 0.4\text{s}$. We note also that the formulae in Granot & Sari (2002) is applicable only in the self-similar phase, which takes a few e-folding times after the deceleration time to fully develop. Our numerical calculation shows that around the deceleration time, the flux should be reduced by a factor of $\sim 2 - 3$. Furthermore, if the deceleration time is not larger than the duration T , the LAT light curve will be flatter at $t < T$, which cannot explain the early-time LAT emission, as discussed in §5 and also strongly argued by Maxham et al. (2011).

The initial jet angle is found to be constrained to be $\theta_j \lesssim 1^\circ$, which implies a collimation-

corrected kinetic energy in the range of short GRBs. We have used for our numerical calculations the semi-analytical jet spreading model of Huang et al. (2000b) (detailed in Appendix A), assuming that the observer line of sight is approximately along the jet axis. This leads us to identify a feature in the late XRT and UVOT light curves as symptomatic of a jet break. We note however that van Eerten et al. (2010) argues that numerically the light curve break related to a jet edge as seen by an off-axis observer may appear hidden for a longer time (weeks) than it would be for an on-axis observer, and the alternative possibility cannot be ruled out, although this being one of the brightest bursts reduces the probability of its being observed from an off-axis direction.

We have considered the origin of the high energy emission under the constraints provided by the low energy observations. Calculation of the Klein-Nishina effect on the IC scattering of synchrotron photons by electrons accelerated in the forward shock indicate that the Klein-Nishina effect suppresses the high energy IC emission significantly, which results in a Y -parameter much smaller than unity. The distribution of the high energy electrons is not affected by the Klein-Nishina effect, so that the synchrotron high energy emission cannot steepen due to a suppression of the IC scattering through Klein-Nishina effects as argued in Wang et al. (2010).

The duration of the prompt emission of this GRB is a crucial parameter for establishing the physics of the LAT emission. Based on the phenomenon that the Fermi GBM emission turns over sharply at $t \sim 0.30 \pm 0.07$ s (De Pasquale et al. 2010), we adopted a duration of $T = 0.30 \pm 0.07$ s, compatible with a thin shell case where the deceleration time is larger than the GRB duration. Here, however, we find that a forward shock synchrotron emission model agrees well only with the late-time ($t > 3$ s) high-energy observations of the LAT, but this model falls well below the early-time high-energy emission (the first six LAT data points). It cannot contribute to the power-law high energy component in the prompt spectrum, which suggests that the early-time high-energy emission may have a different origin from the late-time high-energy emission. We excluded various other possibilities for the early-time high-energy emission, such as synchrotron emission from the reverse external shock, SSC emission from reverse/forward external shock, and IC scattering of forward/reverse synchrotron photons by electrons accelerated in reverse/forward shocks, as well as the high-latitude prompt emission with a small variability timescale. The latter is too steep to contribute to the early-time high-energy emission, due to the assumed high temporal variability of the prompt emission, unless the early-time high-energy emission variability timescale is as large as 0.5 s.

We are led to the conclusion that the early-time high-energy emission is likely due to the final portions of the prompt component, or else to the high latitude component of the prompt emission with a variability time scale as large as 0.5 s plus the synchrotron emission

with a deceleration time $t_{\text{dec}} \leq (2 - 3)\text{s}$. This is supported by the fact that we cannot explain the first six LAT data points by synchrotron forward shock emission if we consider the combined data in the three bands (XRT, UVOT and LAT). In this case, the long-lived high-energy emission can be naturally explained as the result of the prompt emission at early times ($t < (2 - 3)\text{s}$), and the afterglow emission at late times ($t > (2 - 3)\text{s}$) from the adiabatic forward shock synchrotron radiation, with reasonable parameters. In this two-component model of the long-lived high energy emission, the shock deceleration time of $t_{\text{dec}} = 2\text{s}$ results in a fit with an initial Lorentz factor around $\Gamma \simeq 2000$, not much larger than the lower limits $\Gamma_{\text{min}} = 950 \pm 40$ and 1220 ± 60 (Abdo et al. 2009b) obtained from the pair-production limits implied by the presence of 3.4GeV and 31GeV photons. With smaller values of t_{dec} , very large initial Lorentz factors are needed (but see Ioka (2010)). Although there is so far no statistically significant evidence for an early steeper decay, due to the sparse nature of the LAT data, it is striking that by eye there are 4 out of 10 GRB long-lived LAT light curves which have relatively steeper slopes than the slopes, ~ -1 , of typical late-time X-ray and optical afterglows, according to Table 3 and the light curve fits in the figures of Zhang et al. (2010). The steep decay slope of the LAT light curve is difficult to explain with a normal external shock model. A similar conclusion was subsequently suggested by Liu & Wang (2010), and also by Maxham et al. (2011). Our two-component model also explains the steep high-energy temporal decay index values $\alpha_{\text{LAT}} \sim 1.5$ as being the natural result of the superposition of the tail-end of the prompt regime and the start of the afterglow. While our model for the high energy afterglow is in principle applicable to other LAT bursts as well, a homogeneous sample of similarly detailed data including low energy constraints will be needed, on a large number of objects, before definite conclusions can be reached.

We thank D. Burrows, D. Fox, M. De Pasquale, R. Barniol Duran, S. Razzaque, B. Zhang, B.B. Zhang and Y. Z. Fan for useful discussions; Dr. De Pasquale for supplying optical data to us; and the referee for useful comments and suggestions. Partial support was provided by NASA NNX08AL40G, NNX09AT72G, NSF PHY0757155, the NSFC under grants 10973008, the 973 program under grants 2009CB824800, National Natural Science Foundation of China grant 11033002, the Foundation for the Authors of National Excellent Doctoral Dissertations of China, the Program for New Century Excellent Talents in University, the Qing Lan Project and the Fok Ying Tung Education Foundation and China Scholarship Council Postgraduate Scholarship Program.

A. Jet Deceleration and Spreading Dynamical Model

We solve the following equations for the evolution of the shock radius R , the mass m swept up by the shock, the opening half-angle of jet θ and the Lorentz factor of shock Γ (e.g., Huang et al. 2000b).

The evolution of the shock radius is described by

$$\frac{dR}{dt} = \beta c \Gamma (\Gamma + \sqrt{\Gamma^2 - 1}), \quad (\text{A1})$$

with t as the observer’s time and $\beta = \sqrt{\Gamma^2 - 1}/\Gamma$. The swept mass evolves as

$$\frac{dm}{dR} = 2\pi R^2 (1 - \cos \theta) n m_p, \quad (\text{A2})$$

with m_p as the proton mass and n as the number density of surrounding medium. The evolution of the opening angle considering the jet spreading is described as

$$\frac{d\theta}{dt} \equiv \frac{1}{R} \frac{da}{dt} = \frac{c_s (\Gamma + \sqrt{\Gamma^2 - 1})}{R}, \quad (\text{A3})$$

where a is the comoving lateral radius of the jet (Rhoads 1999; Moderski et al. 2000) and the comoving sound speed $c_s = \hat{\gamma}(\hat{\gamma} - 1)(\Gamma - 1) \frac{1}{1 + \hat{\gamma}(\Gamma - 1)} c^2$ with the adiabatic index $\hat{\gamma}$ as $\hat{\gamma} \approx (4\Gamma + 1)/(3\Gamma)$. The conservation of the total energy can be expressed as

$$\frac{d\Gamma}{dm} = - \frac{\Gamma^2 - 1}{M_{\text{ej}} + \eta_r m + 2(1 - \epsilon)\Gamma m}, \quad (\text{A4})$$

where the radiative efficiency is $\eta_r = 0$ for the adiabatic case, and M_{ej} is the ejecta mass.

B. The High-latitude emission

Because photons from high latitude region with respect to the line of sight will arrive later than that from low latitude region due to the curved front surface of the jet, we will observe a fast decreasing emission instead of an abrupt cutoff of the emission, which is so called “curvature effect”.

We neglect the radial structure of the emitting shell for simplicity. Under this assumption we calculate the flux from the shell at radius r_i which expands toward us with Lorentz factor Γ_i by (Granot et al. 1999; Woods & Loeb 1999; Ioka & Nakamura 2001; Yamazaki et al. 2003; Dermer 2004; Toma et al. 2009)

$$F_\nu(t) = \frac{1+z}{d_L^2} 8\pi r_i^3 j'_\nu \frac{1}{[1 + \Gamma_j^2 \theta^2(t)]^2}, \quad (\text{B1})$$

where the photon frequency in comoving frame is

$$\nu' = (1+z)\nu \frac{1 + \Gamma_j^2 \theta^2(t)}{2\Gamma_j} \quad (\text{B2})$$

with ν as the photon frequency in observing frame, and $\theta(t)$ describes the emitting point of the high-latitude emission. We have the comoving emissivity

$$j'_{\nu'} \propto \nu'^{-\beta} \propto (1 + \Gamma_j^2 \theta^2(t))^{-\beta}, \quad (\text{B3})$$

where β is the spectral index of the observed emission, which is consistent with the power-law spectra fit of (Abdo et al. 2009b). By using the relationship $\theta(t) = \sqrt{2} \left[1 - \frac{c}{r_i} \left(\bar{t}_i - \frac{t}{1+z} \right) \right]^{1/2}$ with \bar{t}_i as the emission time in the central engine frame, we get

$$1 + \Gamma_j^2 \theta^2(t) = \frac{t - (t_0 - \Delta t)}{\Delta t} \quad (\text{B4})$$

where $t_0 = (1+z)(\bar{t}_i - \frac{r_i}{c})$ is the observed peak time of the high energy pulse and $\Delta t = \frac{r_i(1+z)}{2c\Gamma_i^2}$ is the observed dynamical time scale. Therefore, the observed flux evolves as time as following

$$F_\nu(t) \propto \left[\frac{t - (t_0 - \Delta t)}{\Delta t} \right]^{-2-\beta}. \quad (\text{B5})$$

REFERENCES

- Abdo, A. A. et al. 2009a, *ApJ*, 706, L138, 0909.2470
- . 2009b, *Nature*, 462, 331, 0908.1832
- . 2010, *ApJ*, 712, 558
- . 2009c, *Science*, 323, 1688
- . 2009d, *ApJ*, 707, 580, 0910.4192
- Achterberg, A., Gallant, Y. A., Kirk, J. G., & Guthmann, A. W. 2001, *MNRAS*, 328, 393, arXiv:astro-ph/0107530
- Ackermann, M. et al. 2010a, *ApJ*, 717, L127, 1007.3409
- . 2010b, *ApJ*, 716, 1178
- Asano, K., Guiriec, S., & Mészáros, P. 2009, *ApJ*, 705, L191, 0909.0306
- Belczynski, K., Perna, R., Bulik, T., Kalogera, V., Ivanova, N., & Lamb, D. Q. 2006, *ApJ*, 648, 1110, arXiv:astro-ph/0601458
- Blandford, R. D., & McKee, C. F. 1976, *Physics of Fluids*, 19, 1130
- Corsi, A., Guetta, D., & Piro, L. 2010, *ApJ*, 720, 1008, 0911.4453
- De Pasquale, M. et al. 2010, *ApJ*, 709, L146, 0910.1629
- Dermer, C. D. 2004, *ApJ*, 614, 284, arXiv:astro-ph/0403508
- Fermi-LAT, & Fermi-GBM collaborations. 2011, ArXiv e-prints, 1101.2082
- Freedman, D. L., & Waxman, E. 2001, *ApJ*, 547, 922, arXiv:astro-ph/9912214
- Gao, W., Mao, J., Xu, D., & Fan, Y. 2009, *ApJ*, 706, L33, 0908.3975
- Ghirlanda, G., Ghisellini, G., & Nava, L. 2010, *A&A*, 510, L7+, 0909.0016
- Ghisellini, G., Ghirlanda, G., Nava, L., & Celotti, A. 2010, *MNRAS*, 403, 926, 0910.2459
- Golenetskii, S. et al. 2009, *GRB Coordinates Network*, 9344, 1
- Granot, J., for the Fermi LAT Collaboration, & the GBM Collaboration. 2010, ArXiv e-prints, 1003.2452

- Granot, J., Piran, T., & Sari, R. 1999, *ApJ*, 513, 679, arXiv:astro-ph/9806192
- Granot, J., & Sari, R. 2002, *ApJ*, 568, 820, arXiv:astro-ph/0108027
- Guiriec, S., Connaughton, V., & Briggs, M. 2009, GRB Coordinates Network, 9336, 1
- Hoversten, E. A., Krimm, H. A., Grupe, D., Kuin, N. P. M., Barthelmy, S. D., Burrows, D. N., Roming, P., & Gehrels, N. 2009, GCN Report, 218, 1
- Huang, Y. F., Dai, Z. G., & Lu, T. 2000a, *MNRAS*, 316, 943, arXiv:astro-ph/0005549
- Huang, Y. F., Gou, L. J., Dai, Z. G., & Lu, T. 2000b, *ApJ*, 543, 90, arXiv:astro-ph/9910493
- Ioka, K. 2010, *Progress of Theoretical Physics*, 124, 667, 1006.3073
- Ioka, K., & Nakamura, T. 2001, *ApJ*, 554, L163, arXiv:astro-ph/0105321
- Kobayashi, S., Zhang, B., Mészáros, P., & Burrows, D. 2007, *ApJ*, 655, 391, arXiv:astro-ph/0506157
- Kumar, P., & Barniol Duran, R. 2009, *MNRAS*, 400, L75, 0905.2417
- . 2010, *MNRAS*, 409, 226, 0910.5726
- Kumar, P., & Panaitescu, A. 2000, *ApJ*, 541, L51, arXiv:astro-ph/0006317
- Liu, R., & Wang, X. 2010, ArXiv e-prints, 1009.1289
- Longo, F. et al. 2009, GRB Coordinates Network, 9343, 1
- Maxham, A., Zhang, B., & Zhang, B. 2011, ArXiv e-prints, 1101.0144
- McBreen, S. et al. 2010, *A&A*, 516, A71+, 1003.3885
- Moderski, R., Sikora, M., & Bulik, T. 2000, *ApJ*, 529, 151, arXiv:astro-ph/9904310
- Nakar, E., Ando, S., & Sari, R. 2009, *ApJ*, 703, 675, 0903.2557
- Neamus, A. 2010, ArXiv e-prints, 1005.1051
- Ohmori, N. et al. 2009, GRB Coordinates Network, 9355, 1
- Rau, A., McBreen, S., & Kruehler, T. 2009, GRB Coordinates Network, 9353, 1
- Razzaque, S. 2010, *ApJ*, 724, L109, 1004.3330
- Rhoads, J. E. 1997, *ApJ*, 487, L1+, arXiv:astro-ph/9705163

- . 1999, *ApJ*, 525, 737, arXiv:astro-ph/9903399
- Sari, R. 1997, *ApJ*, 489, L37+
- Sari, R., & Esin, A. A. 2001, *ApJ*, 548, 787, arXiv:astro-ph/0005253
- Sari, R., Piran, T., & Narayan, R. 1998, *ApJ*, 497, L17+, arXiv:astro-ph/9712005
- Toma, K., Wu, X., & Mészáros, P. 2009, *ApJ*, 707, 1404, 0905.1697
- Toma, K., Wu, X., & Meszaros, P. 2010, ArXiv e-prints, 1002.2634
- Ukwatta, T. N. et al. 2009, GRB Coordinates Network, 9337, 1
- van Eerten, H., Zhang, W., & MacFadyen, A. 2010, *ApJ*, 722, 235, 1006.5125
- Wang, X., He, H., Li, Z., Wu, X., & Dai, Z. 2010, *ApJ*, 712, 1232, 0911.4189
- Wang, X., Li, Z., & Mészáros, P. 2006, *ApJ*, 641, L89, arXiv:astro-ph/0601229
- Wang, X. Y., Dai, Z. G., & Lu, T. 2001, *ApJ*, 546, L33, arXiv:astro-ph/0010320
- Woods, E., & Loeb, A. 1999, *ApJ*, 523, 187, arXiv:astro-ph/9903377
- Yamazaki, R., Yonetoku, D., & Nakamura, T. 2003, *ApJ*, 594, L79, arXiv:astro-ph/0306615
- Zhang, B., Kobayashi, S., & Mészáros, P. 2003, *ApJ*, 595, 950, arXiv:astro-ph/0302525
- Zhang, B. et al. 2010, ArXiv e-prints, 1009.3338

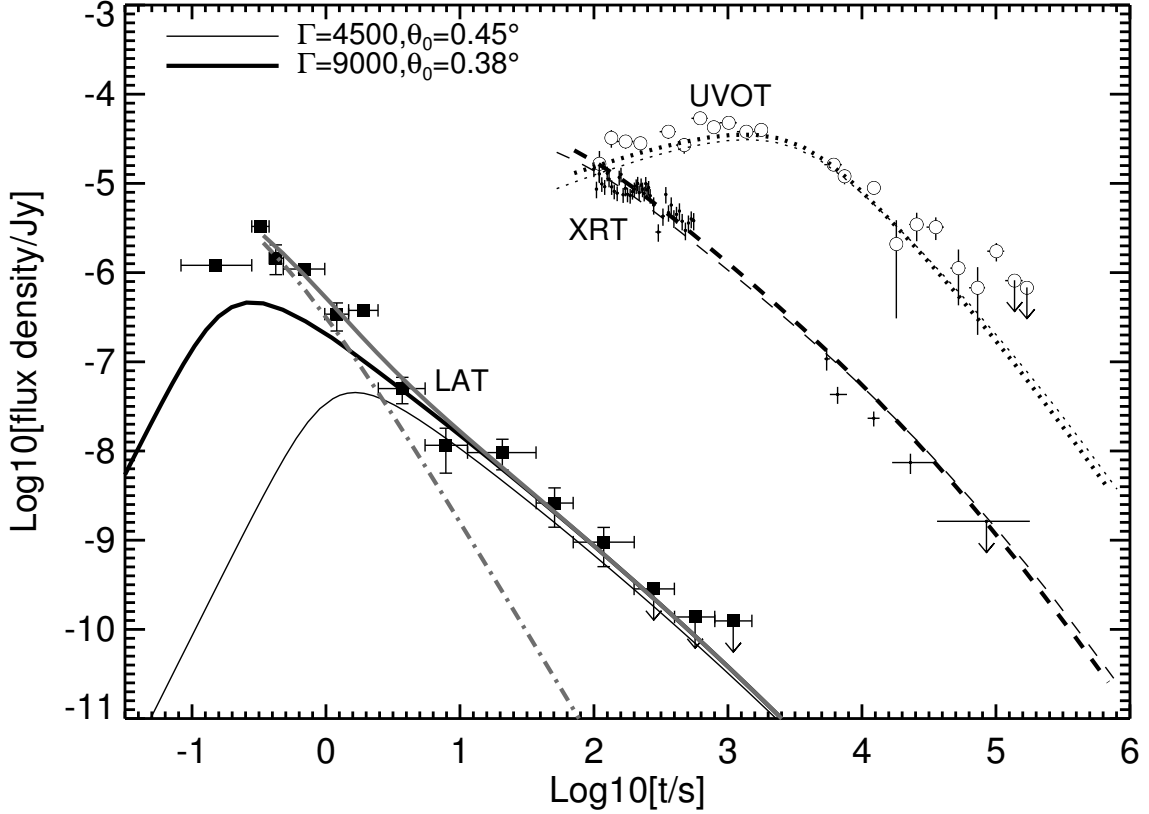


Fig. 1.— GRB 090510 broad-band fitting. The data are the energy flux densities averaged in the observed energy bands (De Pasquale et al. 2010): LAT(100MeV-4GeV, filled squares); XRT (0.2 keV - 10 keV, crosses); UVOT (white band, open circles). The black dotted, dashed and solid lines are the light curves of the optical, X-ray and high energy emission, respectively, from the adiabatic forward shock synchrotron emission in the jet spreading model with parameters $E = 3 \times 10^{53}$ ergs, $\epsilon_e = 0.17$, $\epsilon_B = 7 \times 10^{-3}$, $n = 1 \times 10^{-6}$ cm $^{-3}$ and electron index $p = 2.5$. The thick lines are for an initial Lorentz factor $\Gamma_0 = 9000$ and an initial jet half-angle $\theta_0 = 0.38^\circ$; the thin lines are for $\Gamma_0 = 4500$ and $\theta_0 = 0.45^\circ$. The thick gray dotted line shows a hypothetical component, which can be explained by the high latitude emission of the prompt emission with a variability timescale $\Delta t = 0.5$ s, which makes up for the difference between the synchrotron emission with $\Gamma_0 = 9000$ and the observations. The thick gray solid line is the sum of the thick gray dotted line and the thick black solid line.

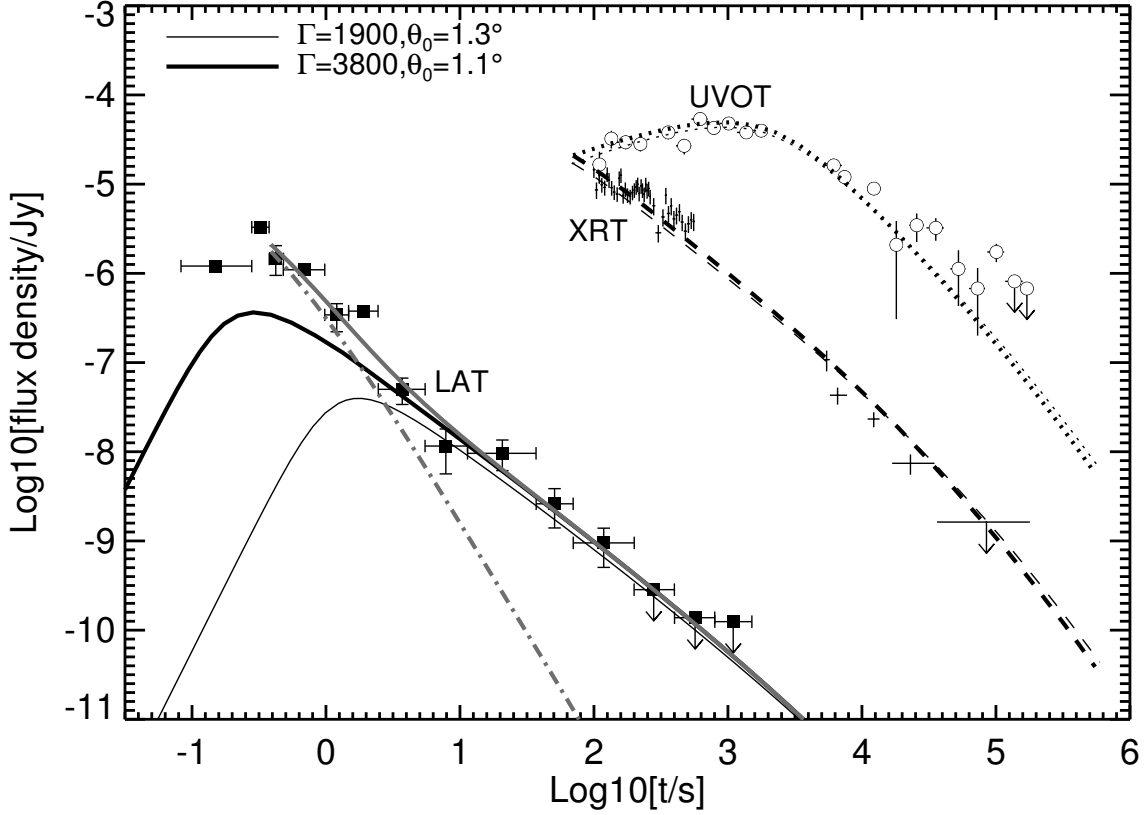


Fig. 2.— GRB 090510 broad-band fitting via the adiabatic forward shock synchrotron emission in the jet spreading model, with parameters $E = 3 \times 10^{53}$ ergs, $\epsilon_e = 0.6$, $\epsilon_B = 10^{-5}$, $n = 10^{-3} \text{cm}^{-3}$ and $p = 2.5$. The thick lines are for an initial Lorentz factor $\Gamma_0 = 3800$ and an initial jet half-angle $\theta_0 = 1.3^\circ$, while the thin lines are for $\Gamma_0 = 1900$ and $\theta_0 = 1.1^\circ$. The thick gray dotted line shows a hypothetical component, which can be explained by the high latitude emission of the prompt emission with a variability timescale $\Delta t = 0.5$ s, which makes up for the difference between the synchrotron emission with $\Gamma_0 = 3800$ and the observations. The thick gray solid line is the sum of the thick gray dotted line and the thick black solid line.